A large impact crater beneath Hiawatha Glacier in northwest Greenland

Kurt Kjær, Nicolaj Larsen, Tobias Binder, Anders Björk, Olaf Eisen, Mark Fahnestock, Svend Funder, Adam Garde, Henning Haack, Veit Helm, et al.

GEOLOGY

A large impact crater beneath Hiawatha Glacier in northwest Greenland

Kurt H. Kjær[1]*, Nicolaj K. Larsen[1,2], Tobias Binder[3], Anders A. Bjørk[1,4,5], Olaf Eisen[3,6], Mark A. Fahnestock[7], Svend Funder[1], Adam A. Garde[8], Henning Haack[9,10], Veit Helm[3], Michael Houmark-Nielsen[1], Kristian K. Kjeldsen[1,8,11], Shfaqat A. Khan[12], Horst Machguth[13,14], Iain McDonald[15], Mathieu Morlighem[4], Jérémie Mouginot[4,16], John D. Paden[17], Tod E. Waight[18], Christian Weikusat[3], Eske Willerslev[1,19,20], Joseph A. MacGregor[21]

We report the discovery of a large impact crater beneath Hiawatha Glacier in northwest Greenland. From airborne radar surveys, we identify a 31-kilometer-wide, circular bedrock depression beneath up to a kilometer of ice. This depression has an elevated rim that cross-cuts tributary subglacial channels and a subdued central uplift that appears to be actively eroding. From ground investigations of the deglaciated foreland, we identify overprinted structures within Precambrian bedrock along the ice margin that strike tangent to the subglacial rim. Glaciofluvial sediment from the largest river draining the crater contains shocked quartz and other impact-related grains. Geochemical analysis of this sediment indicates that the impactor was a fractionated iron asteroid, which must have been more than a kilometer wide to produce the identified crater. Radiostratigraphy of the ice in the crater shows that the Holocene ice is continuous and conformable, but all deeper and older ice appears to be debris rich or heavily disturbed. The age of this impact crater is presently unknown, but from our geological and geophysical evidence, we conclude that it is unlikely to predate the Pleistocene inception of the Greenland Ice Sheet.

INTRODUCTION

The scientific exploration of Greenland has extended for centuries because of its remote location and ice cover. Exploration of features beneath the ice is a relatively new development, owing to the mid-20th century advent of borehole drilling through ice and radar sounding (*1*). While airborne radar sounding of the Greenland Ice Sheet began in the 1970s (*2*), increasingly comprehensive surveying of the ice sheet has only become possible over the past two decades. Beginning in the mid-1990s, extensive airborne radar sounding has revealed a hitherto hidden landscape beneath the Greenland Ice Sheet and elucidated the processes and events that have led to its present bed topography (*3*). Through internal stratigraphy detected by this radar sounding, these data also reveal the late Pleistocene and Holocene history of the ice sheet itself (*4*). Here, we describe a new landscape feature in remote northwest Greenland, initially identified through incidental airborne radar sounding, and subsequently studied through additional airborne and ground-based field studies of the ice sheet and deglaciated foreland.

[1]Centre for GeoGenetics, Natural History Museum, University of Copenhagen, Copenhagen, Denmark. [2]Department of Geoscience, Aarhus University, Aarhus, Denmark. [3]Alfred Wegener Institute, Helmholtz Centre for Polar and Marine Research, Bremerhaven, Germany. [4]Department of Earth System Science, University of California, Irvine, Irvine, CA, USA. [5]NASA Jet Propulsion Lab, Pasadena, CA, USA. [6]Department of Geosciences, University of Bremen, Bremen, Germany. [7]Geophysical Institute, University of Alaska Fairbanks, Fairbanks, AK, USA. [8]Geological Survey of Denmark and Greenland, Copenhagen, Denmark. [9]Maine Mineral and Gem Museum, Bethel, ME, USA. [10]Geobiology and Minerals Section, Natural History Museum, University of Copenhagen, Copenhagen, Denmark. [11]Department of Earth Sciences, University of Ottawa, Ottawa, Ontario, Canada. [12]DTU Space, National Space Institute, Department of Geodesy, Technical University of Denmark, Kongens Lyngby, Denmark. [13]Department of Geosciences, University of Fribourg, Fribourg, Switzerland. [14]Department of Geography, University of Zurich, Zurich, Switzerland. [15]School of Earth and Ocean Sciences, Cardiff University, Park Place, Cardiff, UK. [16]Université Grenoble Alpes, CNRS, INP, Grenoble, France. [17]Center for Remote Sensing of Ice Sheets, University of Kansas, Lawrence, KS, USA. [18]Department of Geosciences and Natural Resources Management (Geology Section), University of Copenhagen, Copenhagen, Denmark. [19]Department of Zoology, University of Cambridge, Cambridge, UK. [20]Wellcome Trust Sanger Institute, Hinxton, Cambridgeshire, UK. [21]Cryospheric Sciences Lab, NASA Goddard Space Flight Center, Greenbelt, MD, USA.
*Corresponding author. Email: kurtk@snm.ku.dk

RESULTS

Bed morphology beneath Hiawatha Glacier

Using data collected between 1997 and 2014 by NASA's Program for Arctic Regional Climate Assessment and Operation IceBridge (*3*), in combination with 1600 km of new airborne radar data collected in May 2016 (Supplementary Materials and Methods), we identified a large circular depression in the bed topography of the Greenland Ice Sheet (Fig. 1). This structure is covered by up to 930 m of ice but has a clear circular surface expression. An elevated rim in the bed topography encloses the relatively flat depression with a diameter of 31.1 ± 0.3 km and a rim-to-floor depth of 320 ± 70 m. In the center of the structure, the bed is raised up to 50 m above the surrounding topography, with five radar-identified peaks that form a central uplift up to 8 km wide. The overall structure has a depth-to-diameter ratio of 0.010 ± 0.002 and is slightly asymmetric, with a gentler slope toward the southwest and maximum depth in the southeast of the structure. Two winding subglacial channels, up to ~500 m deep and ~5 km wide, intersect the southeast flank of the circular structure (Fig. 1). Before entering the structure, the northern channel merges with the southern channel and then spills over a large breach in the structure's rim upon entering the main depression. These channels do not have a recognizable topographic expression within the structure. On the downstream side of the structure, there is a second smaller breach in the northwestern portion of the structure's rim. Ice flows through this second breach to form the tongue-shaped terminus of Hiawatha Glacier. The present ice-sheet margin lies ~1 km past this northwestern rim, and it is the circular depression itself that contains the semicircular ice lobe that extends conspicuously beyond the straighter ice-sheet margin farther southwest.

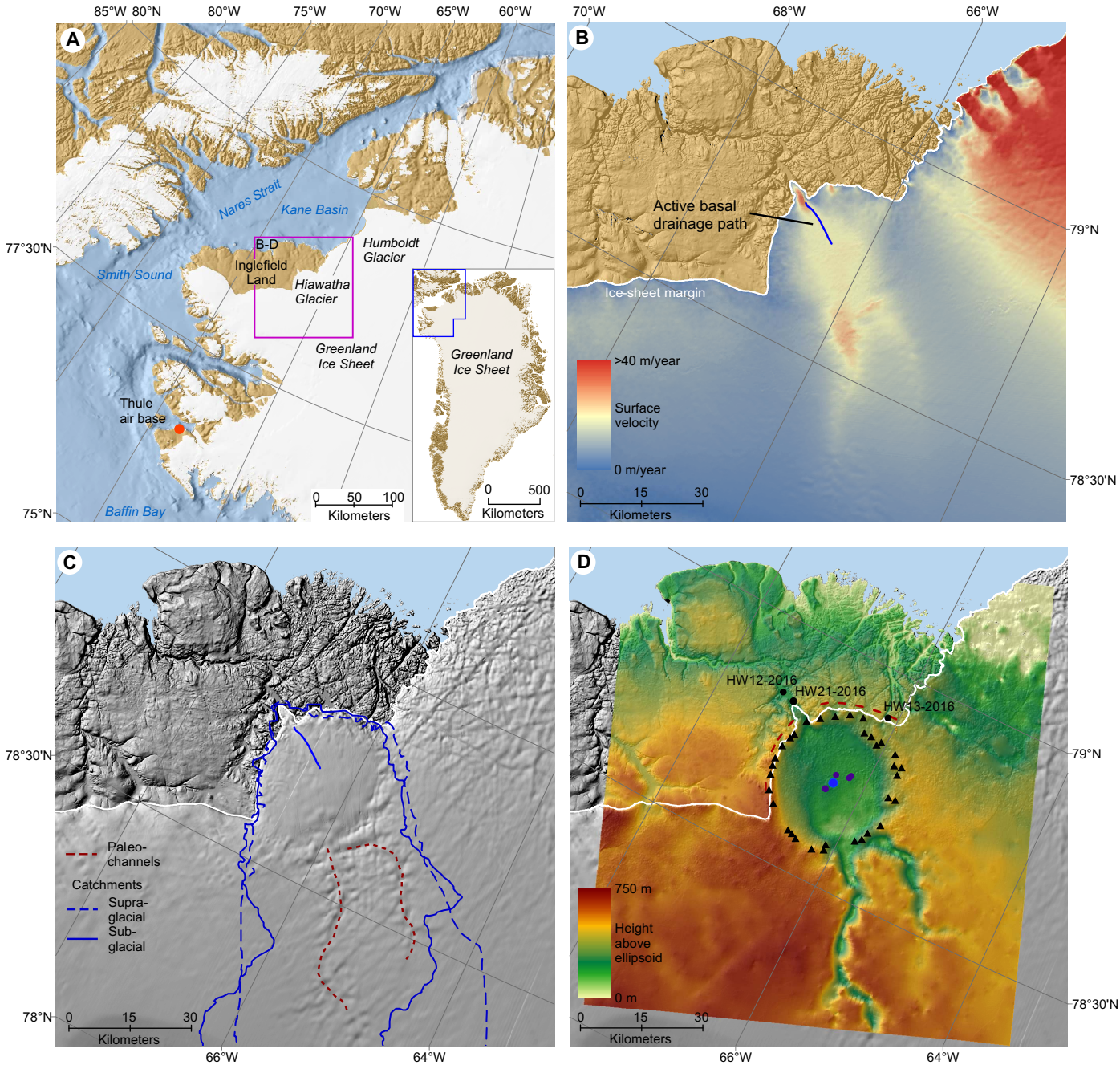

Fig. 1. Geomorphological and glaciological setting of Hiawatha Glacier, northwest Greenland. (**A**) Regional view of northwest Greenland. Inset map shows location relative to whole of Greenland. Magenta box identifies location of (B) to (D). (**B**) A 5-m ArcticDEM mosaic over eastern Inglefield Land. Colors are ice surface velocity. Blue line illustrates an active basal drainage path inferred from radargrams. (**C**) Hillshade surface relief based on the ArcticDEM mosaic, which illustrates characteristics such as surface undulations. Dashed red lines are the outlines of the two subglacial paleochannels. Blue lines are catchment outlines, i.e., solid blue line is subglacial and hatched is supraglacial. (**D**) Bed topography based on airborne radar sounding from 1997 to 2014 NASA data and 2016 Alfred Wegener Institute (AWI) data. Black triangles represent elevated rim picks from the radargrams, and the dark purple circles represent peaks in the central uplift. Hatched red lines are field measurements of the strike of ice-marginal bedrock structures. Black circles show location of the three glaciofluvial sediment samples described in table S1.

Geology of Hiawatha Glacier's foreland

We visited the margin of Hiawatha Glacier in July 2016 to map tectonic structures in the glacier's foreland and to sample its glaciofluvial sediment. The composition of ice-marginal erratic boulders derived from beneath Hiawatha Glacier indicates that the identified structure was formed within the same types of highly metamorphosed Paleoproterozoic terrain as mapped across most of Inglefield Land, which is part of the east-west–trending Inglefield mobile belt (fig. S1) (*5*). The complex tectonic foliation of these ancient rock formations has no clear relation to the present margin of the ice sheet. However, in a narrow zone along

the ice margin, brittle planar structures are superimposed on the bedrock foliation, striking tangentially to the semicircular ice margin around the subglacial circular structure, with moderate to steep outward dips and outward-plunging slickenside lineations (Fig. 1 and fig. S1).

Hiawatha Glacier terminates in a large river that eventually discharges into Nares Strait and is by far the most sediment-rich river discharging from a land-terminating glacier in northwestern Greenland (*6*). Photographic and satellite observations of this terminus over the past century show that distinct active proglacial sedimentation has led to grounding of the initially floating glacier tongue (fig. S2). In 2010, a proglacial outwash floodplain began forming at the terminus and has grown rapidly since (~0.65 km^2 as of 12 September 2016).

Mineralogy and geochemistry of foreland glaciofluvial sediment

Of the three glaciofluvial sediment samples we collected (table S1), only one sample was collected directly from the active floodplain (~2 kg of sand; HW21-2016). In this sample, we found angular quartz grains displaying shock-diagnostic planar deformation features (PDFs) (Fig. 2) (*7*). These PDFs are straight, generally penetrative, and spaced down to less than 2 μm. Only a few are decorated by small fluid inclusions, whereas toasting occurs in some grains (Fig. 3), i.e., a brown coloration due to intense post-shock hydrothermal alteration of the shock lamellae (*8*). The orientations of 37 PDF sets in 10 quartz grains were measured with a five-axis Leitz universal stage. Up to seven different orientations per grain were observed, with {10$\bar{1}$3} and {10$\bar{1}$2} predominating (Fig. 2) (*9*). This distribution is similar to the distribution observed in the central uplifts of large Canadian impact structures, where a threshold shock pressure of >16 GPa was inferred from the presence of {10$\bar{1}$2} PDFs (*10*).

This glaciofluvial sediment sample contains abundant intensely fractured and unweathered grains of detrital K-feldspar, mesoperthite, plagioclase, quartz, sillimanite, garnet, orthopyroxene, rutile, ilmenite, apatite, and other accessory minerals from the local bedrock. We also found a large variety of shock-metamorphosed and glassy grains, along with microbreccias, with sizes between 0.1 and 2 mm (Fig. 3). No larger cobbles or boulders were present at the sampling site of HW21-2016, and so far, none with diagnostic shock-metamorphic effects have been recovered from elsewhere in the foreland.

Several grains consist predominantly or wholly of either glass or variably devitrified glass, as inferred from optical examination and Raman spectroscopy (Figs. 3 and 4 and Materials and Methods). Grain colors are highly variable, ranging from almost colorless to yellow, green, brown, and almost black; glasses with similar bulk compositions may have widely different colors. Major element compositions of glassy grains were determined by electron microprobe (EMP) (data file S1). Unlike typical crustal melts, these grains generally have very low silica contents and commonly yield low analytical totals (~80%), which may be partly affected by poor sample polishing. However, Raman spectroscopy indicates that the glasses with low EMP totals are hydrous and carbon is commonly present. The presence of these elements likely contributes to the low EMP totals. The major element compositions are typically biotite-like (Fig. 3A), garnet-like (Fig. 3, B, G, and H), or feldspar-like (Fig. 3, C, D, L, and N). However, these grains also include appreciable concentrations of elements that do not occur in the respective precursor minerals, such as 2 to 5 weight % (wt %) FeO and up to ~3 wt % MgO in grains with overall feldspar-like compositions, up to ~0.6 wt % CaO in grains with biotite-like compositions, and 0.1 to 0.5 wt % K_2O in grains with garnet-like compositions. Euhedral magmatic microliths of plagioclase, ternary feldspar, orthopyroxene, zoned clinopyroxene, or ilmenite occur in some grains. The Raman spectrum of one glassy grain (Fig. 3A) has small mica bands on a glassy background, a carbon band at ~1600 cm^{-1}, a band indicating organic C–H bonds at ~2900 cm^{-1}, and a band at ~3700 cm^{-1} from mica OH bonds (Fig. 4). Another ellipsoidal grain has a garnet-like composition and a shrinkage crack in the middle and is interpreted to be an intact impact melt droplet (Fig. 3, G and H). Raman and optical spectroscopy of this grain shows that it consists mostly of glass, besides a broad carbon band at ~1600 cm^{-1} (Fig. 4). Very slender radial microliths, recognized by their optical birefringence, are not detected in the Raman spectrum. Other glassy grains have darker rims ~10 μm thick along one or two sides and may be fragments of larger free-falling particles. The carbon bands in the three spectra of Fig. 4 partly or wholly stem from carbon coating, but similar carbon bands also occur in glasses in uncoated mounts.

These glassy grains are interpreted to be derived from impact melting of individual biotite, garnet, and feldspar grains in the metasedimentary bedrock. Their imperfect compositional overlaps with assumed precursor minerals show that the grains do not represent diaplectic glass but instead are variably contaminated mineral melts. Only one grain might approach a bulk rock melt composition (Fig. 3, I and J), as it is siliceous, is highly aluminous (data file S1), and has crystallized Mg-Fe–zoned cordierite microliths besides orthopyroxene and skeletal plagioclase. A Raman spectrum from the matrix displays glass, besides a carbon band at ~1600 cm^{-1}. Bands around ~2900 cm^{-1} are organic C–H bonds, while the band at ~3500 cm^{-1} represents H_2O within the glass. Two other grains contain brown toasted quartz (*11*), with abundant PDFs set in a matrix of devitrified glass with a feldspar-like composition (Fig. 3K) and a structureless mass of carbonaceous material, respectively (Fig. 3M). Another grain displays a shocked quartz fragment with a ballen structure (*12*) set in a glassy matrix of feldspar-like composition with evenly distributed, micaceous crystals only a few micrometers long (Fig. 3, N and O). Microbreccias with matrices of glass, feldspathic microliths, or carbonaceous material are common. The grain shown in Fig. 3 (P and Q) contains fragments of K-feldspar, plagioclase, ilmenite, and quartz in a loosely packed matrix of feldspar microliths. Several quartz areas contain elongate, cusped voids lined with very fine grained clayey material, which might either belong to the sample or be remnants from polishing; the voids themselves are readily distinguished from artifact holes and are interpreted as an original feature, possibly derived from partial vaporization of quartz. Last, the ellipsoidal grain in Fig. 3 (R and S) is black, is soft, and consists of tiny mineral fragments, mainly quartz and feldspar, embedded in a carbonaceous matrix. Some of the mineral fragments outline imperfect ovoid shells that may have formed when the grain was aggregated.

The association of shocked quartz grains mantled by carbonaceous material, microbreccias with amorphous carbonaceous matrix, and glasses with a range of mineral-like compositions is highly unusual for confirmed impact structures, and we are unaware of any directly comparable grain assemblages from these structures. The large morphological and compositional variety of the HW21-2016 grains is unlikely to stem from a homogenized melt sheet on a crater floor. Rather, it probably represents components of the uppermost, unlithified part of an impact structure, and at least a few grains are considered likely to be ejecta (e.g., Fig. 3, G and H).

Subsamples of all three glaciofluvial sediment samples were crushed in an agate mill and analyzed for major and trace elements, platinum-group elements (PGEs), and Au (Materials and Methods and data file S2). Two samples (HW12-2016 and HW13-2016) contain low

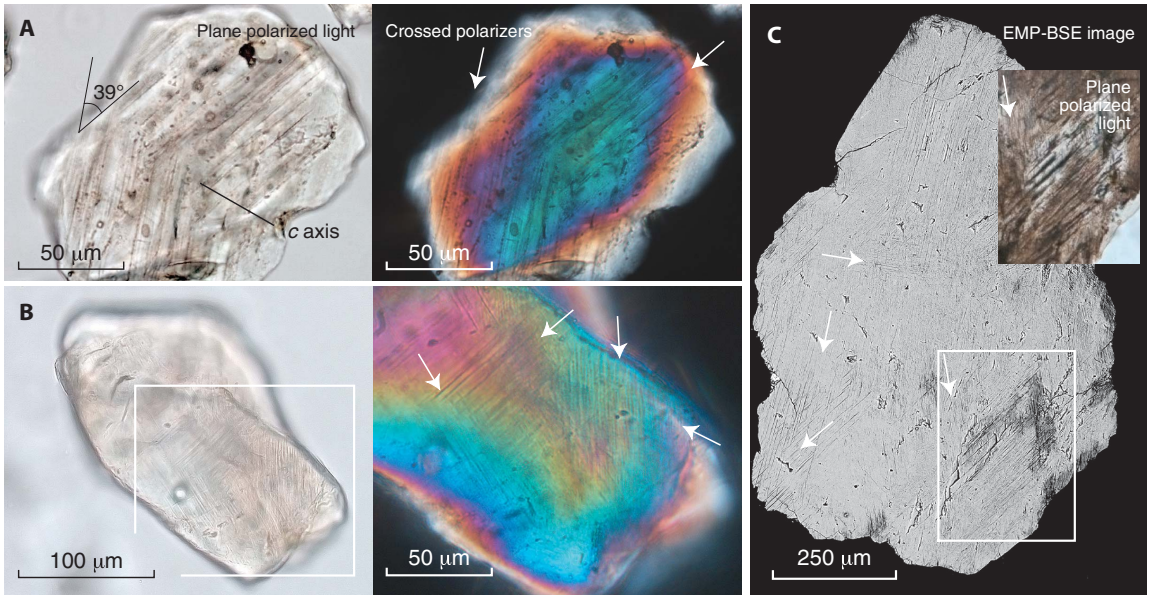

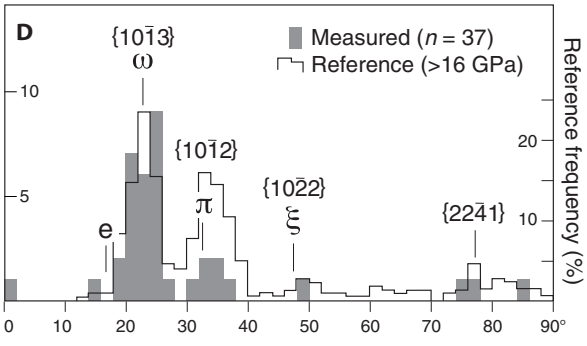

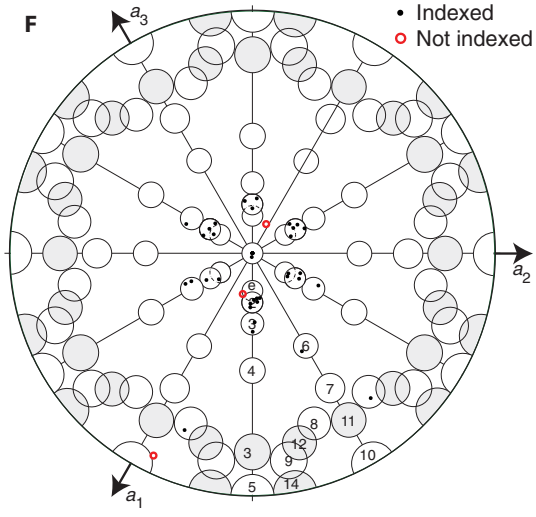

E

Grain	{0001}	{10$\bar{1}$4}	{10$\bar{1}$3}	{10$\bar{1}$2}	{10$\bar{2}$2}	{21$\bar{3}$1}	Not indexed	Sum
Pole angle	0.00	17.62	22.95	32.42	47.73	73.71		
B			2					2
C			1	1			1	3
D			1	3		1	2	7
E			2					2
F			3	2		1		6
G			4		1			5
H			3					3
I			2	1				3
J			3					3
M	1	1	1					3
Sum	1	1	22	7	1	2	3	37
%	3	3	59	19	3	5	8	100

Plane	Pole angle to *c* axis					
1 (0001)	0.00°	**6 {11$\bar{2}$2}**	47.73°	11	{22$\bar{4}$1}	77.20°
2 {10$\bar{1}$3}	22.95°	7	{11$\bar{2}$1} 65.56°	12	{31$\bar{4}$1}	77.91°
3 {10$\bar{1}$2}	32.42°	**8 {21$\bar{3}$1}**	73.71°	13	{40$\bar{4}$1}	78.87°
4	{10$\bar{1}$1} 51.79°	9	{51$\bar{6}$1} 82.07°	14	{51$\bar{6}$0}	90.00°
5	{10$\bar{1}$0} 90.00°	9	{11$\bar{2}$0} 90.00°	e	{10$\bar{1}$4}	17.62°

Fig. 2. Shocked quartz grains from glaciofluvial sediment sample HW21-2016. (**A** to **C**) Microphotographs and backscattered electron (BSE) microscope images of PDFs. (A) Two sets, symmetrical with respect to the optical and crystallographic *c* axis. (B) Four sets. (C) Four closely spaced sets throughout a toasted quartz grain. (**D**) Orientation measurements of 37 sets of PDFs in 10 quartz grains, divided into 2° bins. Reference distribution is for 10 Canadian impact structures with inferred shock pressures >16 GPa (*10*). (**E**) Crystallographic indices of 37 PDF sets in 10 shocked quartz grains, with an average of 3.7 measurable sets per grain. (**F**) Measured quartz PDF orientations in the 10 grains, plotted on a reference net (*9*). The groups of measurements from each grain were rotated on the *c* axis to demonstrate an excellent overall three-dimensional (3D) fit with the 350 reference orientations. Only three sets of PDFs could not be indexed in 3D, although they have permissible angles from the *c* axis.

concentrations of PGE, Au, and other siderophile elements that are consistent with bulk upper continental crust, so those two samples are believed to derive from local bedrock unaffected by the impact (figs. S1 and S3 and Supplementary Materials and Methods). In contrast, every tested subsample of the same sample that contained shocked quartz (HW21-2016) also contains elevated concentrations of Ni, Co, Cr, PGE, and Au, indicative of a relatively rare iron meteorite. PGE data for HW21-2016 produce prominent and consistent chondrite-normalized positive Rh and negative Pt anomalies (fig. S3), and metal ratios are unlike most typical terrestrial rocks that could potentially be local sources for these elevated PGE concentrations (e.g., komatiites, picrites, or high-Mg basalts). Rare sulfide-rich chromitites from the Bushveld Complex have similarly distinctive positive Rh anomalies, but even addition of this material cannot reproduce the observed Rh anomaly. Furthermore, weathering and dispersal of similar rocks would be expected to produce an abundance of Mg-rich and Ti-poor chromite, which is not observed

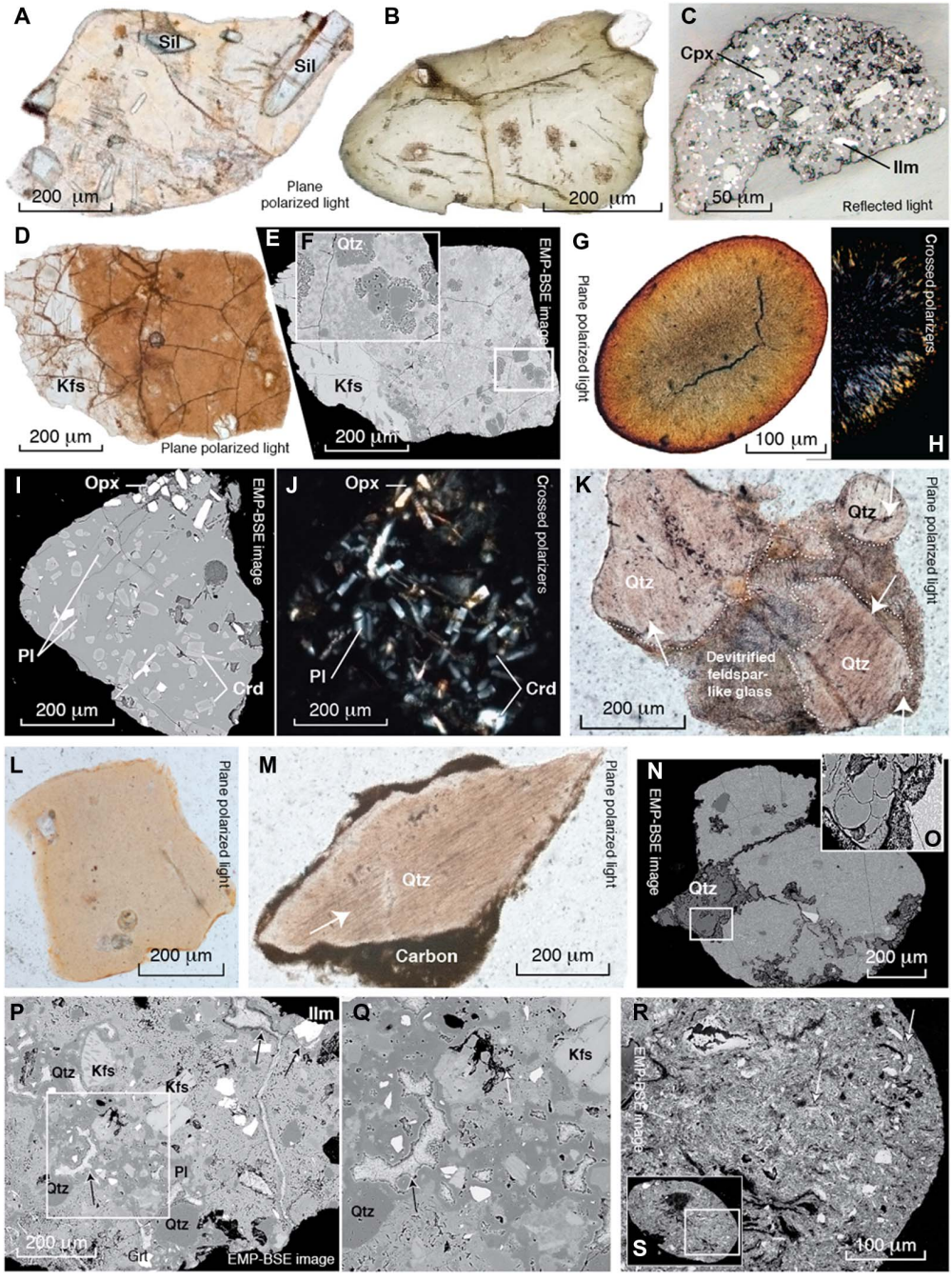

Fig. 3. Impact-related sediment grains from glaciofluvial sediment sample HW21-2016. (**A**) Grain 21C-v32: Pale yellow glass grain of biotite (Bt)–like composition with possibly inherited prismatic sillimanite (Sil) crystals and beginning devitrification in its lower part. (**B**) 21D-u28: Pale green glass grain of garnet (Grt)–like composition with dark rim and beginning devitrification around small trapped mineral fragments. (**C**) 21C-t26: Black glass grain of felsic-like composition with new microporphyritic clinopyroxene (Cpx) and ilmenite (Ilm). (**D** to **F**) 21B-12a: Microperthitic K-feldspar (Kfs) (D) and brown glass of K-feldspar–like composition (E). Inclusions of quartz (Qtz) have acted as nucleation centers for devitrification (F). (**G** and **H**) 21C-z08: Dark brown, ellipsoid glass particle of garnet-like composition with a central contraction crack and beginning crystallization of slender prismatic, radial crystallites. (**I** and **J**) 21C-x20: Pale glass grain of aluminous felsic composition with new microporphyritic orthopyroxene (Opx), zoned cordierite (Crd), and skeletal plagioclase (Pl). (**K**) 21C-u05: Devitrified glass of felsic-like composition with four quartz fragments with PDFs. Arrows indicate prominent PDF orientations. (**L**) 21C-w29: Pale brown glass of K-feldspar–like composition; quartz inclusion with PDFs (top left) and two round inclusions lined with pale micaceous material, possibly former vesicles in the impact mineral melt. (**M**) 21C-z22: Lozenge-shaped, toasted quartz fragment with PDFs throughout, rimmed by black amorphous carbonaceous material. (**N** and **O**) 21D-r06: Quartz fragment with ballen structure (O), set in a matrix of feldspar-like composition with tiny micaceous crystallites. (**P** and **Q**) 21E-p08: Microbreccia with matrix of minute ternary feldspar grains and numerous tiny voids (Q) and inclusions of quartz, K-feldspar, plagioclase, garnet, and ilmenite, and larger elongate, cuspate voids, and channels in quartz (black arrows) with interior linings of clayey material. White arrow in enlargement pointing at a hole from sample preparation, clearly distinguishable from the neighboring original void. (**R**) 21D-u01: Black ellipsoidal grain comprising numerous target mineral fragments and dust in a carbonaceous matrix identified with scanning electron microscopy–energy-dispersive spectrometry and indicated by microprobe totals of only 40 to 70 wt %. (**S**) The entire 21D-u01 grain with hole from polishing.

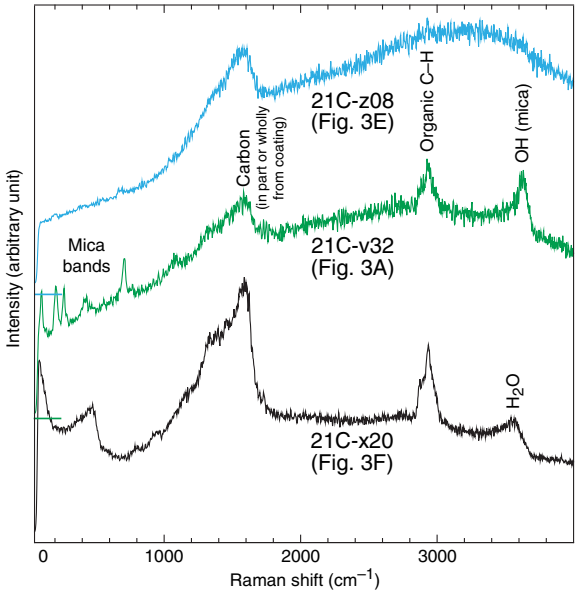

Fig. 4. Raman spectra of glassy matrix of selected grains. Spectra from three grains shown in Fig. 3, with labeled band peaks.

in HW21-2016. The only two recovered spinels are one Cr-poor magnetite and one ilmenite, which have significantly lower MgO, Cr_2O_3, and NiO than spinels found in impact ejecta (*13*). Combinations of PGE ratios in HW21-2016 [e.g., $(Rh/Pt)_N$ >1.2, $(Rh/Ru)_N$ < 0.3, and $(Pd/Pt)_N$ > 2.5] effectively rule out terrestrial rocks and carbonaceous, ordinary, or enstatite chondrites as likely sources, whereas some iron meteorites contain high Rh and Pd concentrations. Modeling indicates that the best fit for the siderophile element data is a mixture between local crust and 0.01 to 0.05% of a component similar in composition to the strongly fractionated Duchesne (type IVA) iron meteorite (fig. S4).

Our examination of the HW21-2016 glaciofluvial sediment sample allows us to conclude three things about its source. First, the shocked quartz grains with multiple PDF orientations very likely originate from a large impact crater upstream from the sampling site. Second, the glassy particles, microbreccias, carbonaceous materials associated with shocked quartz and microbreccias, and grains that are likely ejecta that require a rapidly cooled surficial environment can only be derived from an intact or largely intact crater. Third, the PGE anomalies suggest that these metals derive from a highly fractionated iron asteroid.

Radiostratigraphy of Hiawatha Glacier

In addition to mapping bed topography, the 2016 radar survey also revealed the internal structure of the ice itself. Three major radiostratigraphic units were mapped within and near Hiawatha Glacier (Fig. 5 and movie S1). The upper unit is reflection rich and typically constitutes the upper two thirds of the ice column, with stratigraphic layering that is continuous and conformable across the structure and is observed throughout the Greenland Ice Sheet (movies S2 and S3). Where dated in Greenland ice cores, this radiostratigraphic unit unambiguously represents a complete sequence of Holocene ice [11.7 to 0 thousand years (ka) ago] (fig. S5) (*4*). Where the base of this radar-identified unit outcrops at the ice surface along the margin of Hiawatha Glacier, it corresponds to the top of a distinct, visually dark, and debris-rich band previously identified isotopically as representing the Younger Dryas cold period (12.8 to 11.7 ka ago) at multiple sites across the northern Greenland ice-sheet margin (figs. S2H and S6) (*14*). Above this band, cleaner ice at the surface represents the beginning of the Holocene epoch.

This Holocene ice overlies the second radiostratigraphic unit, which has either poorly expressed or absent stratigraphic layering in the radar data. This reflection-poor unit constitutes the remainder of the ice column outside of the circular bedrock structure and the middle part of the column within it (Fig. 5). This unit must include ice from the Last Glacial Period (LGP; ~115 to 11.7 ka ago). In radar profiles in the northeast corner of the study area, outside the crater, this unit corresponds to late LGP ice exposed at the surface (fig. S6). To the northeast of and within the structure, this unit sits conformably below the Holocene unit, but within the structure, it does not contain any reflection-rich Bølling-Allerød ice (14.7 to 12.8 ka ago), from the period immediately before the Younger Dryas, or the trio of distinct LGP reflections observed throughout the northern Greenland Ice Sheet, the youngest of which is ~38 ka old (fig. S5) (*4*). Instead, those LGP reflections fade and dip noticeably toward Hiawatha Glacier and are absent within ~100 km of it (movies S2 and S3). This second unit does not conform uniformly to the overlying Holocene unit across the entire survey area. In the southern portion of the survey area, its upper interface is exceptionally rough and undulating (movie S1 and fig. S6, C and F to H).

The third unit is basal ice that is thickest in the western half of the survey area, downstream of the center of the structure. This unit contains numerous point scatterers and contiguous bed-originating reflections that tend to initiate at the protruding central peaks within the structure and along its rim (Fig. 5, A, B, E, and F, and movie S1). Radar sounding of the northern Greenland Ice Sheet sometimes detects strong deep reflections that are unlikely to contain significant concentrations of non-ice debris (*4*). However, we interpret the present observations to indicate unusually thick and debris-laden basal ice due to active subglacial erosion and englacial entrainment of mechanically weak subglacial sediment. In support of this interpretation, we note that this unit is mostly detected above the structure itself, and that debris-rich ice outcrops at the front of Hiawatha Glacier, indicating active erosion beneath at least part of the glacier (fig. S2H). We cannot yet directly connect the radar-interpreted top of the basal ice (Fig. 5J) with ground observations of the glacier margin itself (fig. S2H), because this basal ice typically thins substantially as it flows toward the structure's rim (movie S1). The combination of these features, along with the increased small-scale roughness of the bed within the circular structure itself, has not been previously reported by any other radar-sounding survey of an ice sheet.

The ice overlying the downstream half of the structure displays full-column folding of Holocene layering. This folding includes shallow (<100 m depth) and thus recent near-surface layering, and the fold amplitudes are nearly uniform with depth, indicating that active basal processes drive this ice deformation (Fig. 5 and movie S1). Deep synclines in this internal layering (up to ~150 m drawdown relative to adjacent ice) indicate either active and localized basal melting (*15*) or lateral changes in basal drag, but deformation caused by spatial change in basal drag would generate a strain field whose effect upon internal layering would likely decrease in amplitude toward the ice surface (*16*). These full-column synclines correspond to fold patterns at the surface visible where seasonal melting exposes bare ice. These surface patterns show that the hinge line of the most prominent englacial syncline is oriented along ice flow, beginning roughly above the center of the structure and continuing to within a few kilometers of the glacier terminus (Figs. 1B and 5).

Southwest and downstream of the central synclines, an unusual subglacial reflection is observed beneath Hiawatha Glacier that is

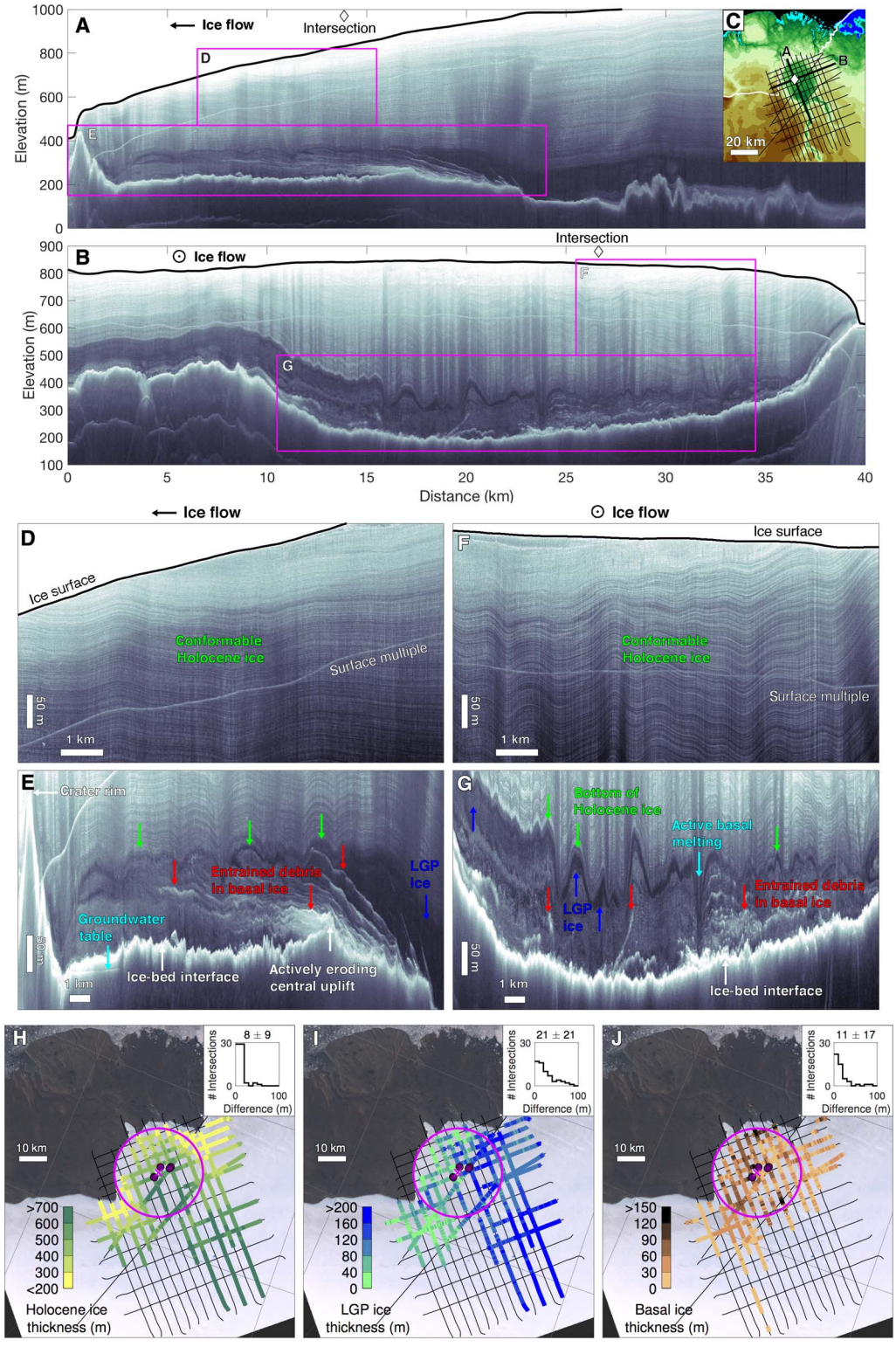

Fig. 5. Radiostratigraphy of Hiawatha Glacier. (**A** and **B**) Example radargrams across Hiawatha Glacier. See movie S1 for all radargrams. The radargram in (A) passes through the subglacial troughs that enter the crater, so the rim there has been fully eroded. (**C**) Map of study area showing location of (A) and (B) overlain on local bed topography. (**D** to **G**) Examples of mapped radiostratigraphic units within Hiawatha Glacier with key features labeled. (**H** to **J**) Thickness of Holocene, LGP, and basal ice within and near Hiawatha Glacier. Background is a natural-color composite Landsat-8 scene from 11 August 2015. Black lines are survey tracks. Units are mapped only where identification is unambiguous. Holocene ice thins as ice flows toward the glacier and is extensively exposed at the ice margin. The incomplete LGP ice sequence thins significantly downstream of the center of the Hiawatha impact crater. Conversely, the apparently debris-rich basal ice thickens significantly downstream of the structure's center. Inset panels show mean, SD, and distribution of the absolute value of crossover thickness differences.

remarkably flat, specular, and clearly not an off-nadir reflection (Fig. 5E and movie S1). This reflection, typically ~15 m beneath the uppermost debris that generates the ice-bed reflection and previously unobserved beneath an ice sheet, is most simply interpreted as the local groundwater table, indicating that the structure's subglacial sediment is water saturated below this level and sufficiently dry above it to permit radar penetration. From examination of high-resolution satellite imagery, most supraglacial rivers that drain into moulins reach close (3 to 8 km) to the Hiawatha Glacier terminus (fig. S7), indicating limited supraglacial meltwater input into the subglacial hydrologic system across most of the structure. On the basis of the above observations and the likely subglacial drainage basin for our survey area (Fig. 1), we conclude that the area beneath Hiawatha Glacier and within the circular structure very likely constitutes the primary sediment source region for the floodplain, where we retrieved the glaciofluvial sediment sample HW21-2016.

DISCUSSION

Identification of the Hiawatha impact crater

We conclude that Hiawatha Glacier is underlain by an impact crater based on the characteristic complex crater morphology beneath the ice (including a subdued central uplift), the rim-tangent structures superimposed on bedrock foliations next to the ice margin, and the fresh, recently deposited glaciofluvial sediment that contains shocked quartz, other impact-related grains, and elevated siderophile element concentrations that our observations strongly suggest originates from beneath Hiawatha Glacier. Other diagnostic impact features, such as shatter cones, are expected to be subglacial in this case; we also have not yet performed a gravity survey across Hiawatha Glacier. Beyond the grains in the sediment sample that we interpret to be possible ejecta, no ejecta layer associated with this structure has yet been identified. Despite the absence of such additional evidence, an impact origin for the structure beneath Hiawatha Glacier is the simplest interpretation of our observations, which we explicitly accept for the remainder of this discussion. This crater is potentially one of the 25 largest impact structures on Earth, and it is the only one of this size that still has a significant portion of its original surface topographic expression.

Preliminary estimates of impactor and ejecta properties

The diameter of an impact crater constrains the kinetic energy of the impactor. The formation of a 31-km-wide impact crater in crystalline target rock requires ~3×10^{21} J of energy (*17*). Assuming that the Hiawatha impactor was iron with a density of 8000 kg m^{-3} and its impact velocity was 20 km s^{-1}, the required impactor diameter was ~1.5 km (*17*). The impact would initially produce a bowl-shaped cavity ~20 km in diameter and ~7 km deep, which would quickly collapse (within ~1 min) to form a complex crater more than 31 km in diameter and ~800 m deep with a central uplift (*17*). This impact scenario would have melted and vaporized up to ~20 km^3 of target rock, approximately half of which would have remained within the crater, forming a melt sheet up to ~50 m deep.

No ejecta layer that might be associated with the Hiawatha impact crater has yet been identified in either Greenland's rock or ice records. If no ice was present at the time of a high-angle (>45°) impact, then the symmetric ejecta layer would be ~200 m thick at the rim, thinning to less than 20 m at a radial distance of 30 km from the rim (*17*). However, during most of the Pleistocene, an ice sheet covered the impact area (*18*). If ice was present and its thickness was comparable to the impactor's diameter, then a more energetic projectile is required to produce a crater of the observed size, and the fraction of non-ice debris in the ejecta would be smaller than if the impact hit ice-free land (*19*). Furthermore, regionally extensive ice cover at the time of impact could have resulted in a significant fraction of the ejecta landing on the ice-sheet surface of the Greenland or Innuitian ice sheets, rather than on bare ground. As the crater is situated very close to the present ice margin, the site has almost certainly been ice free during one or several short (~15 ka) interglacial periods during the Pleistocene, such as predicted for the Eemian ~125 ka ago (*20*). On the basis of present ice-flow speeds (Fig. 1B), most impact ejecta deposited onto the ice sheet would have been transported to the ice margin within ~10 ka. Similarly, based on Holocene vertical strain rates (*21*), any such ejecta would be less than half of its original thickness within 10 ka.

If the Greenland Ice Sheet was present at the time of impact and a high-angle impact occurred during the late Pleistocene (LGP), then ejecta ought to be present in the four deep ice cores from central and northern Greenland that span the majority of the LGP (fig. S5), but none has yet been identified. At two of the ice cores (GISP2 and GRIP) located farthest (>1000 km) from the crater (fig. S5), the expected initial thickness of a symmetric ejecta layer for a Hiawatha-sized impact on rock is ~0.7 mm with an average particle diameter of ~0.4 mm (*17*). In the closer ice cores (fig. S5), this thickness increases roughly twofold. If ice were present at the impact site, then a significant fraction of the ejecta would also be ice (*19*), but the presence of any rock ejecta should be unambiguous in an ice core. A possible complicating factor to interpreting the absence of ejecta in ice cores south of the structure is the presently unknown angle of impact. Modeling indicates that oblique impacts (<45°) produce asymmetric ejecta predominantly downrange of the crater with an ejecta-free shadow zone up range and that this effect becomes more pronounced as the impact angle decreases (*22*). The Hiawatha impact crater is located farther north (78.72°N) than any other known impact crater, a position that increases the probability of a northward-directed oblique impact given the majority of Earth-crossing asteroids that move in or near the ecliptic plane. Such a scenario might be analogous to the late-Jurassic Mjølnir crater, which is also large (40 km diameter), is high latitude (73.8°N), and produced an asymmetric (northward focused) ejecta layer (*23*).

Because it is not yet known whether the Greenland Ice Sheet covered this region at the time of the impact, or its thickness at that time or the impact angle, our estimates of impactor size, initial crater size, impact melt volume, and ejecta thickness and extent should be considered preliminary.

Age of the Hiawatha impact crater

Impact craters on Earth are often dated using radiometric decay systems, but so far, no samples suitable for an absolute age determination have been recovered from the Hiawatha impact crater. We can confidently assume that the structure is younger than the 1.985 to 1.740 Ga old Paleoproterozoic bedrock that outcrops in the immediately adjacent foreland. Furthermore, multiple lines of indirect evidence derived mostly from our radar-sounding survey provide independent, albeit tentative, constraints on the crater's age.

The crater's depth (320 ± 70 m) is muted compared to that predicted for a fresh, subaerial terrestrial crater of the same diameter (~800 m) (*17*, *24*), which could result from either fast erosion over a short period or slower erosion over a longer period. Reported fluvial and subglacial erosion rates span a range of ~10^{-5} to 10^{-2} m $year^{-1}$ (*25*–*28*). An erosion rate at the upper end of that range implies a minimum period of ~5 ka to

erode the rim and central uplift and partially fill the crater floor to form the present morphology, assuming that ice has covered the crater for nearly all of its existence. A lower-end erosion rate yields a loosely constrained maximum erosion period of ~50 Myr. Our radar evidence of active subglacial erosion at present (movie S1) and active sediment deposition at the glacier front (fig. S2) appear to favor a faster subglacial erosion rate and hence a younger age.

The structure's rim cross-cuts and effectively terminates the northern channel east of the crater. The rim also redirects part of the southern channel to its southeast, so we infer that both channels predate the formation of this structure. These two channels are comparable to the paleofluvial channel networks of the neighboring Humboldt Glacier (*29*) and central Greenland's mega-canyon (*30*), which are believed to predate the Pleistocene inception of the Greenland Ice Sheet (~2.6 Ma ago) (*18*). We note that this interpretation requires that the subsequently merged channels later breached the rim itself.

Radar evidence of active basal melting (full-column radiostratigraphic synclines) and subglacial water storage (groundwater table) within and beneath Hiawatha Glacier, respectively, appear to be anomalous as compared to grounded ice-marginal settings across northern Greenland. Possible basal melting could be due to an anomalous subglacial heat source and is consistent with, but not conclusive of, residual heat from the impact itself. Previous modeling of hydrothermal systems within martian subaerial impact craters suggests that such systems have a life span of ~100 ka for a 30-km-wide crater (*31*). For the terrestrial Hiawatha impact crater, the overlying ice sheet would have provided an ample supply of water for such a hydrothermal system during the Pleistocene and Holocene, but it would have also exported heat more efficiently from that system than for a subaerial crater, which suggests a shorter life span of any possible post-impact hydrothermal system than on Mars.

Last, Hiawatha Glacier's radiostratigraphy is highly anomalous compared to the rest of the Greenland Ice Sheet (movies S1 to S3). LGP ice is neither complete nor conformable across the entire crater. Given modern surface velocities (~10 to 30 m year^{-1}) (Fig. 1B), it would only take a few millennia for deeper ice to flow across the crater, so the glacier's age structure cannot yet be clearly explained by steady, uninterrupted ice flow from the ice sheet into the crater. We interpret the deformed radiostratigraphy of this deeper and older ice as indicating that there was a transient that strongly affected ice flow there after most of the LGP ice was deposited. A candidate regional perturbation of ice flow is the retreat of Humboldt Glacier around 9 to 8 ka, which unblocked the Nares Strait (*19*, *32*, *33*). However, surface mapping and dating of moraines, as well as coring in the strait, have not yet shown that this perturbation significantly affected ice flow at the retreating margin (*32*, *34*), so there is no clear reason why that event's effect upon ice flow appears to be focused within and to the south of the Hiawatha impact crater. The anomalous radiostratigraphy could be explained by water pooling subglacially within the topographic depression formed by the preexisting crater, which then outburst catastrophically (and possibly repeatedly) through the rim breach (i.e., a jökulhaup), ultimately affecting local ice flow. Such a scenario requires a significant local or upstream meltwater source, either from basal melting beneath thick ice or from surface melting. Alternatively, the apparent change in ice flow could reflect the ice-sheet response to the impact that formed the crater—if it occurred when ice was present there. Such an impact would have melted, vaporized, and excavated ice locally and would have provided a local heat source that would have continued to melt ice flowing into the crater for an as-of-yet undetermined period post-impact. Between the crater and the local ice divide ~100 km upstream, the ice sheet would have responded to this impact by accelerating, thinning, and transporting the resulting ice and rock ejecta toward the ice margin. At present, we do not have enough evidence to favor one of these hypotheses on the origin of the anomalous LGP radiostratigraphy over the other.

The sum of these tentative age constraints suggests that the Hiawatha impact crater formed during the Pleistocene, as this age is most consistent with inferences from presently available data. An impact before the Pleistocene cannot clearly explain the combination of the relative freshness of the crater's morphology and the ice sheet's apparently ongoing equilibration with the presence of the crater. We emphasize that even this broad age estimate remains uncertain and that further investigation of the age of the Hiawatha impact crater is necessary. Regardless of its exact age, based on the size of the Hiawatha impact crater, this impact very likely had significant environmental consequences in the Northern Hemisphere and possibly globally (*35*).

Significance of the Hiawatha impact crater

No well-preserved impact craters in the upper crust have been found previously in Greenland, partly due to the ice sheet that covers 80% of the island. Our study provides multiple lines of evidence, including high-resolution radar-sounding data and macro- and microscale geologic evidence, of a large crater hidden beneath the ice sheet. The energy needed to generate a 31-km-wide crater could have been produced by a kilometer-scale iron asteroid. While the overall appearance of the Hiawatha impact crater is relatively fresh, its morphological deviations from a typical complex crater are likely due to a combination of glaciofluvial and subglacial erosion of the rim and central uplift, sediment deposition within the crater, and post-impact rim collapse. This crater is the only known terrestrial crater of this size that retains aspects of its original surface topographic expression. The age of the crater is presently unknown, but an impact sometime during the Pleistocene is consistent with presently available geological and geophysical data.

This study suggests several avenues for further research into both the nature and age of the Hiawatha impact crater and other possible subglacial impact craters. In particular, an improved geochronology for this impact event awaits the discovery and analysis of additional samples, from either within the crater itself or the surrounding area. One of the most promising regions is southwest of the crater itself, which appears to be debris rich both englacially and subaerially (*36*). Evidence of ejecta (or lack thereof) north of the structure and its chronostratigraphy could test at least part of the Pleistocene age range and the oblique impact scenario we infer. The consequences of possible impacts into ice masses are sometimes considered for extraterrestrial bodies, but rarely so for Earth. Modeling of both the dynamics of large impacts into an ice sheet, the post-impact modification of crater morphology by flowing ice masses, and the internal structure of those ice masses could help better understand the evolution of the Hiawatha impact crater.

MATERIALS AND METHODS

Radar system, data acquisition, and processing

The ultrawideband chirp radar, developed by the Center for Remote Sensing of Ice Sheets, was operated on AWI's Polar 6, a Basler BT-67 aircraft. The system hardware is an improved version of a previous design (*37*). It consists of three eight-element antenna arrays, operating in the frequency range of 150 to 520 MHz, with a 10-kHz pulse repetition frequency. One array is mounted under the fuselage, and the two others

under each wing. The center array both transmits and receives signals, while the wing arrays receive only. The total transmit power is 6 kW.

Three flights were performed out of Thule Air Base on 12, 16, and 17 May 2016 (movie S1) at a height of ~350 m over the ice sheet, corresponding to an elevation range of 1000 to 2000 m. Before the flights, the amplitude, time delay, and start phase of each element of the transmit array were adjusted to correct for system amplitude, time delay, and phase errors (*37*). The received return signals were filtered at radio frequencies before digitization at 1600 MHz. Each channel was digitally down-converted to complex baseband, decimated to 400 MHz, and then stacked in hardware. For this survey, each of the 24 channels recorded 19,612 complex samples at 294 Hz.

Post-flight processing included a matched filter application for pulse compression in the vertical range direction, equalization to minimize sidelobes, focused synthetic aperture radar (SAR) processing in the along-track direction using an *f-k* migration adapted for radar sounding of ice (*38*), and array processing in the across-track direction after time, amplitude, and phase equalization of each SAR image (*37*). We assumed that the value for the real part of the relative permittivity of ice is 3.17 to convert englacial travel times to depth.

To detect the ice-bed interface and visualize coherent and incoherent backscatter, we used fully SAR and array-processed data from the central eight elements. This process results in a range resolution of 0.5 m and an azimuth resolution of 15 m. Bed topography was calculated by subtracting the ice thickness from the surface elevation available from the Greenland Ice Mapping Project (*39*). To improve the detection and visualization of coherent and incoherent internal backscatter, data from four segments were fully SAR and array processed using the center array, resulting in an improved range resolution (0.5 m) and azimuth resolution (~2.5 m) near the ice-bed interface.

Raman spectroscopy of glaciofluvial sediment

The Raman spectra were obtained with a WITec alpha300 R system, using a 488-nm laser, an UHTS300 spectrometer with a grating of 600 grooves mm^{-1}, a Peltier-cooled electron multiplying charge-coupled device detector, and a long working distance 50× microscope objective with a numerical aperture of 0.35. The instrument was calibrated using the Raman spectrum of a monocrystalline silicon wafer. Laser power was adjusted individually for each sample to prevent heat-induced damage. Acquisition times ranged between 5 and 30 s per spectrum, with 5 to 10 spectra combined for each spot, depending on the signal intensity.

Geochemistry of glaciofluvial sediment

Three glaciofluvial sediment samples were collected from the outwash plain in front of Hiawatha Glacier (HW12-2016, H13-2016, and HW21-2016). All three samples were geochemically analyzed for major elements, trace elements, PGEs, and Au using existing instrumentation and methods (*40*).

Three types of material were provided from the original HW21-2016 bulk sample. HW21-2016(1) was a subsample of ~60 g, which had already been processed for petrographic work, HW21-2016(2) was a subsample of ~30 g of the untreated sediment, and HW21-2016(3) was a subsample of 50 g of untreated sediment that had been sieved to between 63 and 200 μm. A fraction of this latter subsample was split into <125-μm and >125-μm sub-subsamples to determine the major and trace element chemistry of both the fine and coarse material separately. From samples HW12-2016 and HW13-2016, we took ~30 g of untreated subsamples of the original bulk sediment collected at these localities. Each subsample was crushed and homogenized to fine powder at Cardiff University in an agate planetary ball mill. Aliquots of 12 to 15 g of each crushed and homogenized sample were taken to determine PGE and Au concentrations. For each subsample, 0.1-g portions were analyzed for major and trace elements. Major and trace element data, PGE data, and Au data are all provided in data file S2. Subsample HW21-2016(1)B* has significantly higher PGE concentrations than the other HW21-2016 subsamples, pointing to the heterogeneous nature of the siderophile-rich component in the sediment. Mean concentrations are calculated with and without this sample included in data file S2.

SUPPLEMENTARY MATERIALS

Supplementary material for this article is available at http://advances.sciencemag.org/cgi/content/full/4/11/eaar8173/DC1

Supplementary Text
Fig. S1. Bedrock type and lineations across Inglefield Land near Hiawatha Glacier.
Fig. S2. Terminus history of Hiawatha Glacier and its transition from a floating to a grounded tongue with a proglacial floodplain.
Fig. S3. CI-chondrite–normalized metal patterns for glaciofluvial sediment samples compared to upper continental crust.
Fig. S4. Model mixtures of crust with mass proportions of various meteorites.
Fig. S5. Radar reflectivity at the six deep Greenland ice-core sites, as measured by predecessor radar systems to that used for the Hiawatha Glacier survey.
Fig. S6. Relationships between surface and radar layering.
Fig. S7. Supraglacial drainage of Hiawatha Glacier.
Table S1. Location and description of Hiawatha glaciofluvial sediment samples.
Movie S1. The 2016 AWI airborne radar survey over Hiawatha Glacier.
Movie S2. Operation IceBridge radar surveys across the Greenland Ice Sheet.
Movie S3. Operation IceBridge radar surveys toward Hiawatha Glacier.
Data file S1. EMP data for grains studied from HW21-2016 samples.
Data file S2. Major element, trace element, and PGE concentrations for subsamples and sub-subsamples of HW21-2016.
References (*41*–*44*)

REFERENCES AND NOTES

1. G. D. Q. Robin, S. Evans, J. T. Bailey, Interpretation of radio echo sounding in polar ice sheets. *Philos. Trans. R. Soc. A* **265**, 437–505 (1969).
2. P. Gudmandsen, Layer echoes in polar ice sheets. *J. Glaciol.* **15**, 95–101 (1975).
3. M. Morlighem, E. Rignot, J. Mouginot, H. Seroussi, E. Larour, Deeply incised submarine glacial valleys beneath the Greenland Ice Sheet. *Nat. Geosci.* **7**, 418–422 (2014).
4. J. A. MacGregor, M. A. Fahnestock, G. A. Catania, J. D. Paden, S. Prasad Gogineni, S. K. Young, S. C. Rybarski, A. N. Mabrey, B. M. Wagman, M. Morlighem, Radiostratigraphy and age structure of the Greenland Ice Sheet. *J. Geophys. Res. Earth Surf.* **120**, 212–241 (2015).
5. R. Lahtinen, A. Garde, V. Melezhik, Paleoproterozoic evolution of Fennoscandia and Greenland. *Episodes* **31**, 20–28 (2008).
6. I. Overeem, B. D. Hudson, J. P. M. Syvitski, A. B. Mikkelsen, B. Hasholt, M. R. van den Broeke, B. P. Y. Noël, M. Morlighem, Substantial export of suspended sediment to the global oceans from glacial erosion in Greenland. *Nat. Geosci.* **10**, 859–863 (2017).
7. D. Stöffler, F. Langenhorst, Shock metamorphism of quartz in nature and experiment: I. Basic observation and theory. *Meteoritics* **29**, 155–181 (1994).
8. L. Ferrière, G. R. Osinski, Shock metamorphism, in *Impact Cratering: Processes and Products*, G. R. Osinski, E. Pierazzo, Eds. (John Wiley & Sons, 2012), pp. 106–124.
9. L. Ferrière, J. R. Morrow, T. Amgaa, C. Koeberl, Systematic study of universal-stage measurement of planar deformation features in shocked quartz: Implications for statistical significance and representation of results. *Meteorit. Planet. Sci.* **44**, 925–940 (2009).
10. P. B. Robertson, R. A. F. Grieve, Shock attenuation at terrestrial impact structures, in *Impact and Explosion Cratering*, D. J. Roddy, R. O. Papin, R. B. Merrill, Eds. (Pergamon Press, 1977), pp. 687–702.
11. N. M. Short, D. P. Gold, Petrography of shocked rocks from the central peak at the Manson impact structure, in *The Manson Impact Structure, Iowa: Anatomy of an Impact Crater*, C. Koeberl, R. R. Anderson, Eds. (Special Paper 302, Geological Society of America, 1996), pp. 245–265.

12. L. Ferrière, C. Koeberl, W. U. Reimold, Characterization of ballen quartz and cristobalite in impact breccias: New observations and constraints on ballen formation. *Eur. J. Mineral.* **21**, 203–217 (2009).
13. S. Goderis, B. M. Simonson, I. McDonald, S. W. Hassler, A. Izmer, J. Belza, H. Terryn, F. Vanhaecke, P. Claeys, Ni-rich spinels and platinum group element nuggets condensed from a Late Archean impact vapour cloud. *Earth Planet. Sci. Lett.* **376**, 87–98 (2013).
14. N. Reeh, H. Oerter, H. H. Thomsen, Comparison between Greenland ice-margin and ice-core oxygen-18 records. *Ann. Glaciol.* **35**, 136–144 (2002).
15. M. Fahnestock, W. Abdalati, I. Joughin, J. Brozena, P. Gogineni, High geothermal heat flow, basal melt, and the origin of rapid ice flow in central Greenland. *Science* **294**, 2338–2342 (2001).
16. R. W. Jacobel, A. M. Gades, D. L. Gottschling, S. M. Hodge, and D. L. Wright, Interpretation of radar-detected internal layer folding in West Antarctic ice streams. *J. Glaciol.* **39**, 528–537 (1993).
17. G. S. Collins, H. J. Melosh, R. A. Marcus, Earth Impact Effects Program: A Web-based computer program for calculating he regional environmental consequence of a meteoroid impact on Earth. *Meteorit. Planet. Sci.* **40**, 817–840 (2005).
18. P. R. Bierman, J. D. Shakun, L. B. Corbett, S. R. Zimmerman, D. H. Rood, A persistent and dynamic East Greenland Ice Sheet over the past 7.5 million years. *Nature* **540**, 256–260 (2016).
19. L. E. Senft, S. T. Stewart, Impact crater formation in icy layered terrains on Mars. *Meteorit. Planet. Sci.* **43**, 1993–2013 (2008).
20. A. Born, K. H. Nisancioglu, Melting of Northern Greenland during the last interglaciation. *Cryosphere* **6**, 1239–1250 (2012).
21. J. A. MacGregor, W. T. Colgan, M. A. Fahnestock, M. Morlighem, G. A. Catania, J. D. Paden, S. P. Gogineni, Holocene deceleration of the Greenland Ice Sheet. *Science* **351**, 590–593 (2016).
22. V. Shuvalov, Ejecta deposition after oblique impacts: An influence of impact scale. *Meteorit. Planet. Sci.* **46**, 1713–1718 (2011).
23. V. V. Shuvalov, H. Dypvik, Ejecta formation and crater development of the Mjølnir impact. *Meteorit. Planet. Sci.* **39**, 467–479 (2004).
24. H. J. Melosh, *Impact Cratering: A Geologic Process* (Oxford Univ. Press, 1989), 245 pp.
25. M. N. Koppes, D. R. Montgomery, The relative efficacy of fluvial and glacial erosion over modern to orogenic timescales. *Nat. Geosci.* **2**, 644–647 (2009).
26. T. Cowton, P. Nienow, I. Bartholomew, A. Sole, D. Mair, Rapid erosion beneath the Greenland ice sheet. *Geology* **40**, 343–346 (2012).
27. A. Strunk, M. F. Knudsen, D. L. Egholm, J. D. Jansen, L. B. Levy, B. H. Jacobsen, N. K. Larsen, One million years of glaciation and denudation history in west Greenland. *Nat. Commun.* **8**, 14199 (2017).
28. N. E. Young, J. P. Briner, J. Maurer, J. M. Schaefer, ^{10}Be measurement in bedrock constrain erosion beneath the Greenland Ice Sheet margin. *Geophys. Res. Lett.* **43**, 11708–11719 (2016).
29. S. J. Livingstone, W. Chu, J. C. Ely, J. Kingslake, Paleofluvial and subglacial channel networks beneath Humboldt Glacier, Greenland. *Geology* **45**, 551–554 (2017).
30. J. L. Bamber, M. Siegert, J. Griggs, S. Marshall, G. Spada, Paleofluvial mega-canyon beneath the central Greenland Ice Sheet. *Science* **341**, 997–999 (2013).
31. O. Abramov, D. A. Kring, Impact-induced hydrothermal activity on early Mars. *J. Geophys. Res.* **110**, E12S09 (2005).
32. A. E. Jennings, C. Sheldon, T. M. Cronin, P. Francus, J. Stoner, J. Andrews, The Holocene history of Nares Strait: Transition from glacial bay to Arctic-Atlantic throughflow. *Oceanography* **24**, 26–41 (2011).
33. K. L. Knudsen, B. Stabell, M.-S. Seidenkrantz, J. Eiríksson, W. Blake Jr., Deglacial and Holocene conditions in northernmost Baffin Bay: Sediments, foraminifera, diatoms and stable isotopes. *Boreas* **37**, 346–376 (2008).
34. S. Funder, K. K. Kjeldsen, K. H. Kjær, C. Cofaigh, The Greenland ice sheet during the last 300.000 years: A review. *Dev. Quat. Sci.* **15**, 699–713 (2011).
35. C. R. Chapman, D. Morrison, Impacts on the Earth by asteroids and comets: Assessing the hazard. *Nature* **367**, 33–40 (1994).
36. T. Risbo, H. Pedersen, *Kap York-Meteoritekspeditionen* (Carlsberg Foundation, 1994).
37. Z. Wang, S. Gogineni, F. Rodriguez-Morales, J.-B. Yan, J. Paden, C. Leuschen, R. D. Hale, J. Li, C. L. Carabajal, D. Gomez-Garcia, B. Townley, R. Willer, L. Stearns, S. Child, D. Braaten, Multichannel wideband synthetic aperture radar for ice sheet remote sensing: Development and the first deployment in Antarctica. *IEEE J. Sel. Top. Appl. Earth Obs. Remote Sens.* **9**, 980–993 (2016).
38. C. Leuschen, S. Gogineni, D. Tammana, SAR processing of radar echo sounder data, in *IEEE 2000 International Geoscience and Remote Sensing Symposium* (IEEE, 2000) pp. 2570–2572.
39. I. M. Howat, A. Negrete, B. E. Smith, The Greenland Ice Mapping Project (GIMP) land classification and surface elevation data sets. *Cryosphere* **8**, 1509–1518 (2014).
40. I. McDonald, K. S. Viljoen, Platinum-group element geochemistry of mantle eclogites: A reconnaissance study of xenoliths from the Orapa kimberlite, Botswana. *Appl. Earth Sci.* **115**, 81–93 (2006).
41. L. Koch, *Contributions to the Glaciology of North Greenland* (Meddelelser om Grøonland, 1928).
42. S. M. McLennan, Relationships between the trace element composition of sedimentary rocks and the upper continental crust. *Geochem. Geophys. Geosys.* **2**, 2000GC000109 (2001).
43. J.-W. Park, Z. Hu, Z. Gao, I. H. Campbell, H. Gong, Platinum group element abundances in the upper continental crust revisited—New constraints from analyses of Chinese loess. *Geochim. Cosmochim. Acta* **93**, 63–76 (2012).
44. K. Lodders, Solar system abundances and condensation temperatures of the elements. *Astrophys. J.* **591**, 1220–1247 (2003).

Acknowledgments: We thank the Carlsberg and Mamont Foundations for supporting this study and NASA Operation IceBridge, the NSF Arctic Program, Kenn Borek Air, and Thule Air Base for helping make the AWI radar survey possible. ArcticDEM was created by the Polar Geospatial Center from DigitalGlobe Inc. imagery. N. Henriksen (Oskar) supported the project from the early start and provided the regional context for an impact crater to have occurred in the region. S. T. Jørgensen of Air Greenland provided excellent support during intense fieldwork along the Hiawatha Glacier in the summer of 2016. AWI contributed in-kind (material, personnel, data storage, and computing) to acquiring the radar. **Funding:** This work is a part of Centre for GeoGenetics supported by the Danish National Research Foundation (DNRF94). K.K.K. acknowledges support from the Danish Council Research for Independent research (grant no. DFF-4090-00151). A.A.B. acknowledges support from the Danish Council for Independent Research (grant no. DFF-610800469) and by the Inge Lehmann Scholarship from the Royal Danish Academy of Science and Letters. We acknowledge NSF award 1129716 for development of the radar system and the University of Kansas for development of the radar software. Villum Foundation and Aarhus University Research Foundation supported N.K.L. Last, we thank the Polar Geospatial Center for their ArcticDEM and geospatial support provided via NSF PLR awards 1043681, 1559691, and 1542736. **Author contributions:** N.K.L. and A.A.B. noted the conspicuous topographic depression upstream the Hiawatha Glacier. K.H.K. led the subsequent study. K.H.K., N.K.L., O.E., J.A.M., M.A.F., H.M., H.H., and E.W. designed the study and conducted and interpreted the results. T.B., V.H., and J.D.P. performed the AWI radar survey and processed the data. J.A.M., O.E., M.A.F., J.D.P., T.B., and V.H. interpreted the radar data. A.A.G., H.H., I.M., T.E.W., and C.W. performed the microstructural and geochemical analyses of sediment grains. K.H.K., S.F., K.K.K., M.H.-N., A.A.G., H.H., H.M., J.M., N.K.L., and A.A.B. conducted the ground-based and remote-sensing surveys of Inglefield Land. K.H.K. drafted the manuscript, and all co-authors contributed, discussed, and commented on it. **Competing interests:** The authors declare that they have no competing interests. **Data and materials availability:** All data needed to evaluate the conclusions in the paper are present in the paper and/or the Supplementary Materials. Additional data related to this paper may be requested from the authors.

Submitted 20 December 2017
Accepted 9 October 2018
Published 14 November 2018
10.1126/sciadv.aar8173

Citation: K. H. Kjær, N. K. Larsen, T. Binder, A. A. Bjørk, O. Eisen, M. A. Fahnestock, S. Funder, A. A. Garde, H. Haack, V. Helm, M. Houmark-Nielsen, K. K. Kjeldsen, S. A. Khan, H. Machguth, I. McDonald, M. Morlighem, J. Mouginot, J. D. Paden, T. E. Waight, C. Weikusat, E. Willerslev, J. A. MacGregor, A large impact crater beneath Hiawatha Glacier in northwest Greenland. *Sci. Adv.* **4**, eaar8173 (2018).

A large impact crater beneath Hiawatha Glacier in northwest Greenland

Kurt H. Kjær, Nicolaj K. Larsen, Tobias Binder, Anders A. Bjørk, Olaf Eisen, Mark A. Fahnestock, Svend Funder, Adam A. Garde, Henning Haack, Veit Helm, Michael Houmark-Nielsen, Kristian K. Kjeldsen, Shfaqat A. Khan, Horst Machguth, Iain McDonald, Mathieu Morlighem, Jérémie Mouginot, John D. Paden, Tod E. Waight, Christian Weikusat, Eske Willerslev and Joseph A. MacGregor

Sci Adv **4** (11), eaar8173.
DOI: 10.1126/sciadv.aar8173